Article

Titanium nitride sensor for selective NO$_2$ detection

Xuefei Zhao [1], Zhihang Xu [2], Zhaorui Zhang[1,3], Jiahao Liu[1], Xiaohui Yan[1], Ye Zhu[2], J. Paul Attfield [4] & Minghui Yang [1] ✉

Efficient detection methods are needed to monitor nitrogen dioxide (NO$_2$), a major NO$_x$ pollutant from fossil fuel combustion that poses significant threats to both ecology and human health. Current NO$_2$ detection technologies face limitations in stability and selectivity. Here, we present a transition metal nitride sensor that exhibits exceptional selectivity for NO$_2$, demonstrating a sensitivity 30 times greater than that of the strongest interfering gas, NO. The sensor maintains stability over 6 months and does not utilize platinum or other precious metals. This notable performance has been achieved through preparation of highly active titanium nitride (TiN$_x$) nanoparticles with exceptionally large surface area and a high concentration of nitrogen vacancies. By contrast, a commercial sample of TiN shows no gas sensing activity. Such devices are potentially scalable for everyday NO$_2$ detection and demonstrate that robust high-performance gas sensors based on inexpensive metal nitrides without precious metals are leading candidates for environmental monitoring technologies.

Nitrogen dioxide (NO$_2$) is listed among the six primary air pollutants by both the U.S. Clean Air Act and the World Health Organization (WHO)[1,2], and is widely recognized as a primary culprit in triggering asthma and other respiratory diseases[3]. However, 99% of the global population is exposed to air that fails to meet the WHO standard, leading to significant public health deficits[4]. Therefore, monitoring NO$_2$ pollution in the air is crucial for protecting public health. The US Environmental Protection Agency (EPA) has set the annual average safe concentration of NO$_2$ in ambient air at 53 ppb, with over 117 countries actively participating in air quality monitoring using various gas sensors[4,5].

Several technologies for measuring low atmospheric concentrations of NO$_2$ are available, but all have some limitations. Metal oxide semiconductors like SnO$_2$ and ZnO have poor selectivity and do not perform well under high humidity and at low temperatures[6]. Electrochemical sensors based on precious metals such as platinum (Pt) offer high performance but are costly and lack long-term stability due to

detachment and aggregation of Pt nanoparticles during extended operation[7,8]. Recent research on incorporating quantum dots into gels has been shown to enhance surface area and increase availability of active sites but duration is limited to <100 h[9]. Single-atom catalyst sensors offer active sites at the atomic level, but are challenged by low synthesis efficiency and poor stability[10].

In this work, we focus on transition metal nitrides (TMNs), which hold significant potential for sensing applications due to their high electronic conductivity and chemical stabilities[11]. Recent studies have demonstrated that TMNs act as active supports for Pt-based sensing of several pollutant gases such as H$_2$S, CO and formaldehyde[12–14]. Furthermore, one study found that nitriding In$_2$O$_3$ improves NO$_2$ sensing performance without use of Pt[15]. This has motivated the present study to design a highly active TMN sensor for NO$_2$. We have chosen TiN as this material has been extensively studied as a stable and highly conducting TMN[16,17]. TiN is widely used as a durable coating and also occurs naturally as the mineral osbornite[18]. Our initial explorations

[1]School of Environmental Science and Technology, Dalian University of Technology, Dalian, China. [2]Department of Applied Physics, Research Institute for Smart Energy, The Hong Kong Polytechnic University, Hung Hom, Hong Kong, China. [3]School of Mechanical Engineering, State Key Laboratory of High-performance Precision Manufacturing, Dalian University of Technology, Dalian, China. [4]Centre for Science at Extreme Conditions and School of Chemistry, University of Edinburgh, Edinburgh, UK. ✉e-mail: myang@dlut.edu.cn

showed that commercial TiN is inactive (see later results for TiN-CM sample), so we focused on developing more active materials by introducing nitrogen vacancies (NVs) to increase surface activity, and by nanostructuring to increase surface area. Several methods such as molten-salt synthesis[19], solid-solid separation[20], and the urea-glass route[21] are used to prepare nanostructured TMNs, but these methods do not yield sufficiently active TiN surfaces for NO_2 sensing. High temperatures (over 600 °C) or pressures are needed to generate NVs[16,22], so our strategy has been to synthesize TiN_x through the high-temperature ammonolysis of a metal-organic framework (MOF) precursor, **MIL-125**(Ti)[23]. The resulting TiN_x exhibits the highest surface area reported for a TMN and high levels of NVs (up to 20%), leading to notable sensor performance without use of Pt. We have also used spectroscopic methods to demonstrate that the NO_2 sensing mechanism occurs through the $NO_2 \rightarrow NO_2^- \rightarrow NO$ reduction sequence.

Results and discussion
Samples preparation and characterization
We synthesized TiN_x via ammonolysis of MOF **MIL-125** (Ti), retaining its high surface area and forming abundant NVs around metal sites (Figs. S1, S2). The powder X-ray diffraction (XRD) patterns confirmed successful synthesis at various temperatures, designated as TiN-500 to TiN-900 whose properties were compared with those of a commercial sample TiN-CM (Fig. S3, Table S1). The MOF-derived TiN-600 nanoparticles exhibited a significantly high specific surface area of 221.9 m²/g (Fig. 1a, S4, S5, Table S2), 90 times that of TiN-CM. The High-Resolution Transmission Electron Microscopy (HRTEM) image showed

lattice fringes of the (331) and (400) planes of TiN-600 (Fig. S6a), indicating randomly oriented grains. The scanning electron microscopy (SEM) images (inset of Fig. S6a) confirmed the uniform square morphology consistent with **MIL-125** (Fig. S6b). Electron Energy-Loss Spectroscopy (EELS) elemental mapping images and Energy Dispersive Spectrometer (EDS) mapping images verified the homogeneous distribution of N and Ti elements in TiN (Fig. S7–S11).

The X-ray photoelectron spectroscopy (XPS) results indicate a 0.11 eV negative shift in the Ti 2p peak of TiN-600, and an increased peak intensity of N 1s (attributed to NVs) compared to TiN-900, suggesting a lower oxidation state of Ti in TiN-600 and a higher concentration of NVs (Fig. S12)[24]. We subsequently conducted element-sensitive synchrotron radiation X-ray absorption spectroscopy (XAS) measurements to investigate the local coordination of NVs at the atomic level. The X-ray absorption near-edge structure (XANES) spectrum (Fig. 1b) shows that the near-edge absorption energy of TiN-600 is negatively shifted compared to TiN-CM, indicating a slight decrease in average Ti oxidation state due to NVs formation[25], which is consistent with the Ti 2p XPS observations. The local coordination of NVs at the atomic level was studied through Fourier transform extended X-ray absorption fine structure (EXAFS) analysis. As shown in Fig. S13, the Ti-N bond intensity in TiN-600 is weaker compared to TiN-CM, indicating a reduction in the Ti-N coordination number[24], increased NVs[26], thus providing strong evidence for the formation of NVs. Discontinuous lattice stripes and blurred or missing lattice sites in the filtered image (Fig. 1c) indicate the presence of vacancy defects. These vacancies can function as active centers, thereby increasing catalytic activity[27]. The corresponding
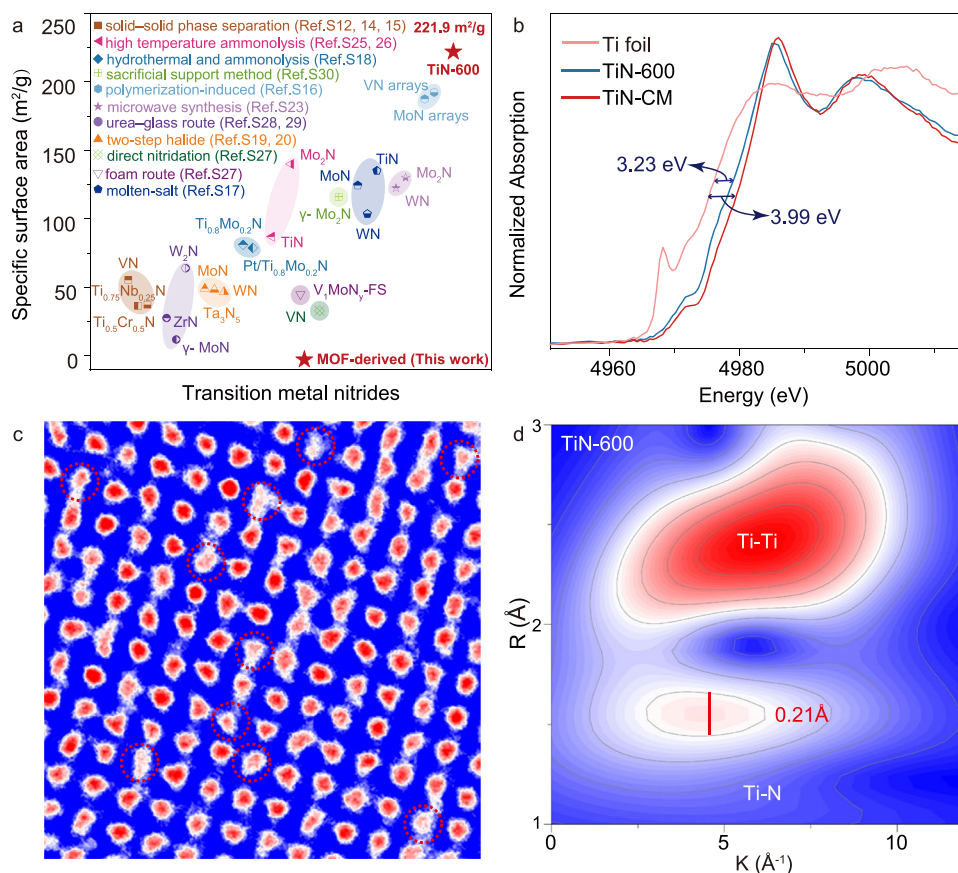

Fig. 1 | High surface area TiN_x with abundant nitrogen vacancies (NVs) derived from MOF. a A comparison of the MOF-derived transition metal nitride (TMNs) synthesis method with previously reported methods for enhancing the specific surface area of TMNs. References in the plot can be found in the Supplementary Information. **b** The K-edge X-ray absorption near edge structure (XANES) of TiN- 600, TiN-CM, and Ti foil. **c** High-resolution transmission electron microscopy (HRTEM) filtered image of the area within the square in Fig. S6a. The red circles represent NVs. **d** The wavelet transform curve of and TiN-600. Source data are provided as a Source Data file.
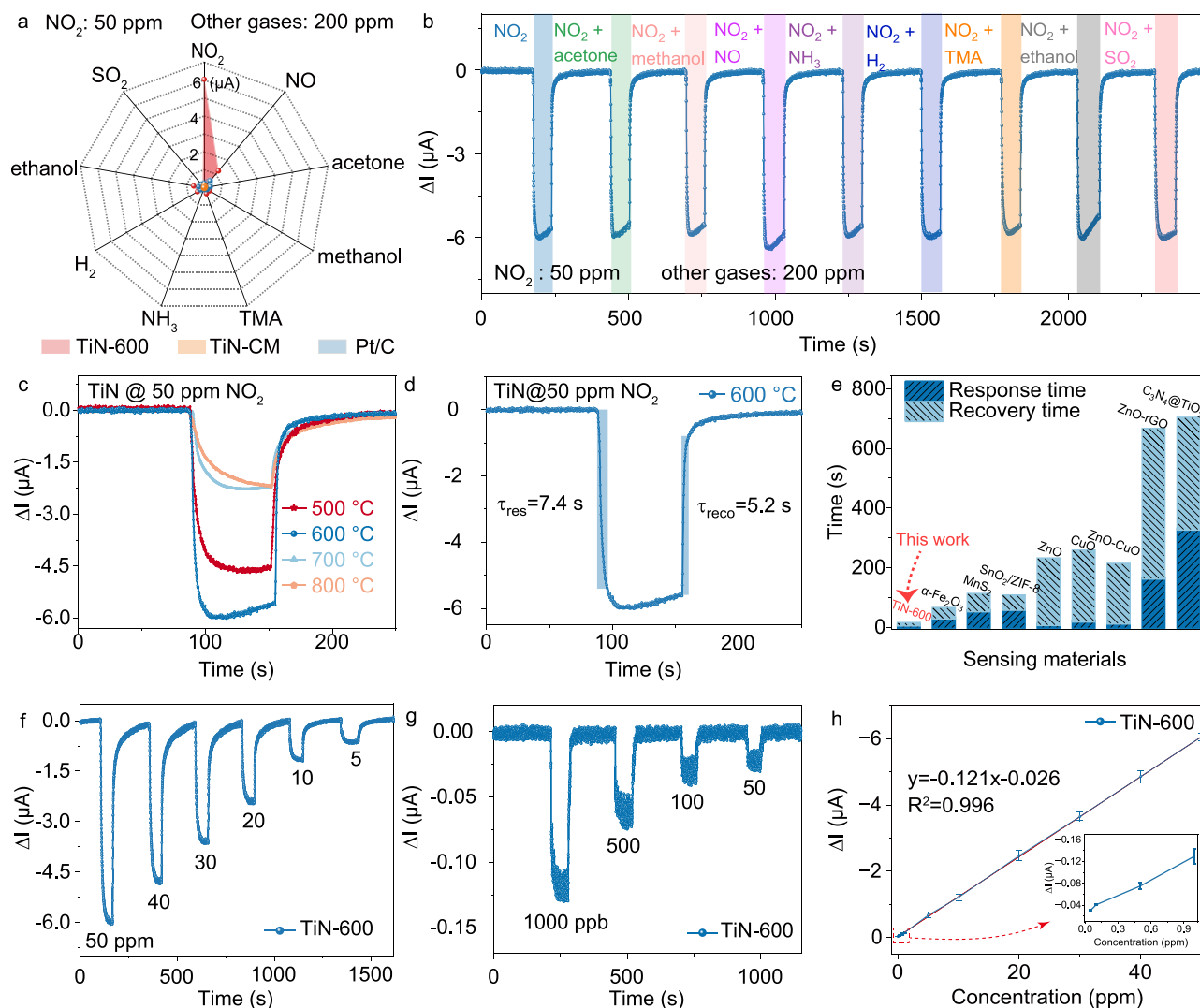
Fig. 2 | The selectivity, response-recovery characteristics, and response-concentration correlation of TiN$_x$ sensors. a Selectivity of TiN-600, TiN-CM, and Pt/C sensors toward various analyte gases. **b** Sensor response of TiN-600 to a transient of 50 ppm nitrogen dioxide (NO$_2$), followed by eight transients of mixed gases (50 ppm NO$_2$ with 200 ppm acetone, methanol, nitric oxide (NO), ammonia (NH$_3$), hydrogen (H$_2$), trimethylamine (TMA), ethanol and sulfur dioxide (SO$_2$), respectively). **c** The response transients of TiN-500, TiN-600, TiN-700 and TiN-800 sensors to 50 ppm NO$_2$. **d** Response recovery transient curve of TiN-600 sensor to 50 ppm NO$_2$. **e** Summary of the response and recovery times of NO$_2$ gas sensors. **f, g** Real-time responses and **h** NO$_2$ concentration dependent response value of TiN-600 sensor to 0.05–50 ppm NO$_2$. Error bars represent the standard deviation of at least three independent measurements. Source data are provided as a Source Data file.

wavelet transform EXAFS contour plots for TiN-600 and TiN-CM show that the intensity maximum of the Ti-N bond at k ≈ 4.5 Å^{-1} in TiN-600 (Fig. 1d) is significantly reduced compared to TiN-CM (Fig. S14), further indicating the presence of NVs. A series of EPR experiments showed a clear pair of peaks at g = 2.003 in TiN-600 (Fig. S15), indicating the presence of unpaired electrons[28,29]. The high intensity of these EPR signals reflects the concentration of unsaturated sites with unpaired electrons, thereby confirming the abundant formation of NV centers in the TiN-600 material. This phenomenon is closely related to its gas-sensing response[25,30].

Gas sensing performance

Selectivity, a critical parameter for assessing gas sensor performance, is evaluated by recording the current changes of the sensor in different concentrations and types of gases. As shown in Fig. 2a and S16, the response of TiN-600 to NO$_2$ is substantially higher than that of TiN-CM and Pt/C sensors. Figure 2b further demonstrates that the responses to various interfering gases, including 200 ppm NO, acetone, methanol,

trimethylamine (TMA), ammonia (NH$_3$), hydrogen (H$_2$), sulfur dioxide (SO$_2$) and ethanol, are negligible. Density functional theory (DFT) calculations for the adsorption behavior of different gases on the surface of TiN-NVs, indicate that the adsorption energy of NO$_2$ on TiN-NVs (−4.61 eV) is significantly higher than that of other gases (see Figs. S17 and S18). This suggests a stronger interaction between NO$_2$ and TiN-NVs. Additionally, the geometric parameters of the above gas molecules in both adsorbed and free states on TiN-NVs were optimized (Table S3). The distance between N and O atoms in the NO$_2$ molecule (d_{N-O}) and the intrinsic NO$_2$ bond angle (∠ONO) were analyzed, revealing that when NO$_2$ is adsorbed on TiN-NVs, d_{N-O} is 1.452 Å, and ∠ONO is 110.1°. Therefore, the geometric parameters of the NO$_2$ molecule change more significantly upon adsorption on TiN-NVs compared to other gases, which can be explained by ion-dipole interactions[31]. The increased changes in geometric parameters indicate lower resistance to electron transfer from NO$_2$ to TiN-NVs[32]. The stronger interaction and more significant charge transfer between NO$_2$ and TiN-NVs reflect the superior selectivity of the sensor for NO$_2$. In
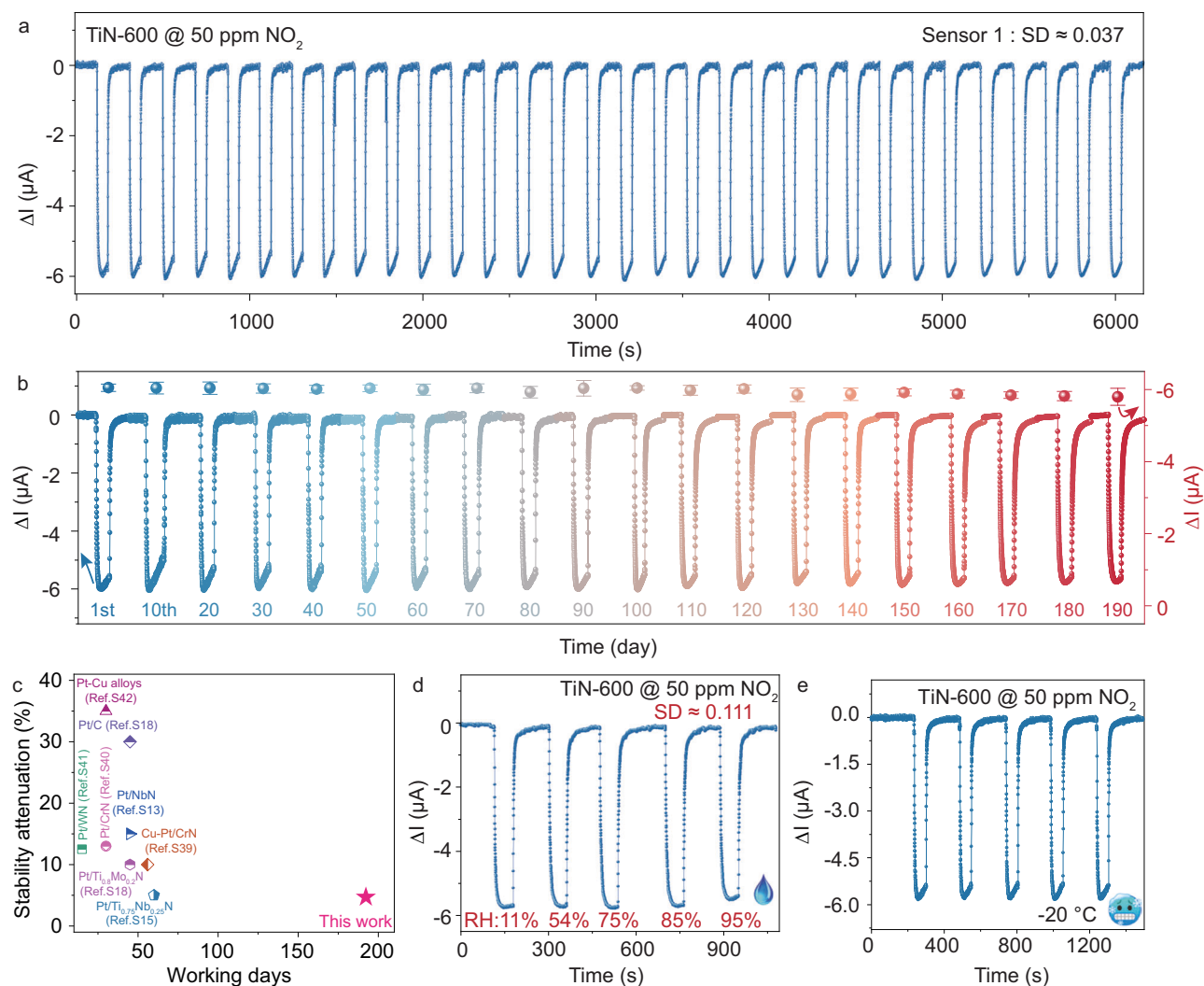
Fig. 3 | The stability and environmental tolerance of TiN$_x$ sensors. a 30-cycle dynamic sensing response of TiN-600 sensor to 50 ppm NO$_2$. **b** The response of the TiN-600 sensor to 50 ppm NO$_2$ decreased by only 4.2% over 6 months. **c** Comparison of the long-term stability of the TiN-600 sensor with previously reported Pt-loaded electrochemical gas sensors. References in the plot can be found in the Supplementary Information. **d** The effect of different relative humidities (RH) on the transient response of the TiN-600 sensor. **e** The dynamic sensing response of the TiN-600 sensor to 50 ppm NO$_2$ at −20 °C. Source data are provided as a Source Data file.

contrast, the changes in geometric parameters (like $d_{N–O}$ and $\angle ONO$) for other gases adsorbed on TiN-NVs are minimal. This indicates weak interactions with the material surface, resulting in lower sensitivity to these gases.

To determine the optimal ammonolysis reaction temperature, we evaluated the gas-sensing properties of a series of TiN samples by monitoring their responses to NO$_2$. As shown in Fig. 2c, TiN-600 exhibited the highest response to NO$_2$, with response and recovery times of 7.4 s and 5.2 s, respectively (Fig. 2d), which are the fastest among the TiN samples (Fig. S19). An interesting trend was observed between the specific surface areas of TiN synthesized at different ammonia treatment temperatures and their responses to NO$_2$: the sensor response was proportional to the specific surface area (Table S4). Additionally, we summarized the response and recovery times of different types of gas sensors to NO$_2$ (Fig. 2e, S20, Table S5), demonstrating again the advantage of using MOF-derived methods to prepare high specific surface area samples for sensing applications. Moreover, the response of the TiN-600 sensor quickly reaches a peak after exposure to NO$_2$ and then slightly decreases (Fig. 2d). This behavior may result from the rapid occupation of active sites by NO$_2$ during initial exposure, leading to a swift rise in the sensor's response.
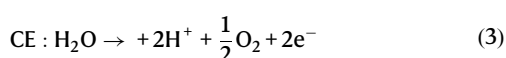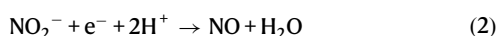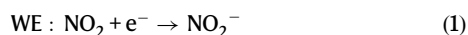
The subsequent slight decline in the response signal could be attributed to the sensor's self-recovery mechanism, which allows for partial desorption after a certain amount of NO$_2$ is adsorbed. This mechanism prevents sensor failure due to prolonged exposure to high concentrations of NO$_2$. The TiN-600 sensor exhibits a positive linear response to NO$_2$ in the range of 50 ppb to 50 ppm (Fig. 2f, g), with a sensitivity of 0.12 μA/ppm (Fig. 2h), and a Limit of Detection (LoD) as low as 50 ppb, which is capable of detecting the minimum concentration set by the EPA (53 ppb)[5]. Additionally, the baseline current of the sensor operating in air for 30 min was recorded (Fig. S21), and the low current fluctuations facilitate the identification of the sensor response signal. Based on the Root Mean Square Deviation (RMSD) method[33], the theoretical LoD of the TiN-600 sensor is determined to be 2.4 ppb.

A series of TiN sensors demonstrated excellent cyclic stability (Fig. 3a and S22), with the TiN-600 sensor showing nearly fluctuation-free response when repeatedly tested for 30 cycles in 50 ppm NO$_2$, with a standard deviation (SD) of approximately 0.037 μA. In addition, we validated the reproducibility of TiN-600 sensors from different batches (Fig. S23). Considering the practical applications of the TiN-600 gas sensor, a dynamic sensing response monitoring over

6 months was conducted. It was found that the response decreased by only 4.2% compared to the first day, indicating excellent long-term stability of the TiN-600 sensor (Fig. 3b). In previous studies, researchers have attempted to enhance gas sensor response by loading Pt onto the sensitive materials. However, this approach has often resulted in poor long-term stability of the gas sensors (Fig. 3c and Table S6). To investigate the impact of relative humidity (RH) on the gas-sensing performance of the sensor, gases with varying humidity levels were prepared using the saturated salt solution method. Figure S24 shows that the impact of RH on baseline current is minimal, with fluctuations in different humidity environments being even lower than the current bias, a result validated by previous studies[20,34]. Fig. 3d depicts the transient response to 50 ppm NO_2 under different humidity conditions. SD of the response at various humidity levels is 0.111 μA, indicating the response current of the sensor is minimally affected by humidity. Furthermore, the response and recovery times of the TiN-600 sensor demonstrate minor variation under different RH (Fig. S25). This stability may be attributed to the small sealed water reservoir in the counter electrode (CE), which assists in maintaining a relatively constant humidity level and reduces sensitivity to changes in external RH. Therefore, the TiN-600-based electrochemical gas sensor successfully addresses the issue of poor environmental tolerance in chemical resistive gas sensors caused by the competitive adsorption of water molecules and oxygen molecules at active adsorption sites[35]. Given the significant practical importance of detecting gases in low-temperature environments such as cold winters, polar regions, and refrigerated storage, which is rarely addressed and achieved in current NO_2 sensors, we have investigated the low-temperature sensing characteristics of the TiN-600 sensor. Notably, even when the operating temperature is reduced to −20 °C, the sensor response to NO_2 decreases by only 2.7% compared to the response at RT (Fig. 3e). This may be due to the plentiful NVs in TiN-600, whose concentration is temperature independent and which function as active reaction sites and reduce the activation energy[36], thereby lessening the impact of temperature on the gas sensing reaction rate. The slight decrease in response can be primarily attributed to the reduced electrochemical reactivity and slower reaction dynamic of the material at sub-zero temperatures[37]. Additionally, the response of the TiN-600 sensor to NO_2 is nearly identical whether nitrogen or air is used as the background gas (Fig. S26). This may be attributed to the negligible impact of oxygen concentration on the response[38].

Gas sensing mechanism

The proposed gas-sensing mechanism of the TiN-600 electrochemical gas sensor is depicted in Fig. 4a. When the working electrode (WE) contacts with NO_2 molecules, a reduction reaction occurs, producing the intermediate NO_2^- (reaction (1)). The NO_2^- can further be reduced to NO under acidic conditions (reaction (2))[39]. Simultaneously, an oxidation reaction takes place at the CE (reaction (3)), generating protons (H^+) that migrate through the Nafion membrane to the WE. The generated electrons (e^-) cannot pass through the Nafion membrane and instead are transferred to the WE via an external circuit. This electron transfer in the external circuit results in a detectable current signal.

$$WE: NO_2 + e^- \rightarrow NO_2^- \tag{1}$$

$$NO_2^- + e^- + 2H^+ \rightarrow NO + H_2O \tag{2}$$

$$CE: H_2O \rightarrow +2H^+ + \frac{1}{2}O_2 + 2e^- \tag{3}$$

In-situ monitoring of NVs in TiN-600 is essential for understanding the adsorption mechanism of the material. As shown in Fig. 4b, the EPR signal intensity of TiN-600 decreases over time after NO_2 adsorption. This decay is due to the formation of a gas layer on the material surface caused by gas molecule adsorption[40–42]. This process enhances spin-lattice interactions, resulting in a weakened EPR signal. Moreover, as the number of adsorbed gas molecules increases, the gas layers become thicker and denser, further contributing to the attenuation of the EPR signal[43]. Understanding the rapid dynamic equilibrium exchange between surface species and the gas phase is essential for designing efficient catalyst desorption systems. Building on previous work and the hypothesis ($NO_2 + 2e^- + 2H^+ = NO + H_2O$)[38], we further investigated the NO_2 sensing reaction process using in-situ FTIR spectroscopy to provide a more comprehensive mechanism (Fig. S27). During NO_2 catalysis on the TiN-600 catalyst, characteristic vibrational peaks at 1200 cm^{-1} and 1219 cm^{-1} were attributed to NO_2^- and bridging nitrite, respectively (Fig. 4c)[44,45]. Additionally, Fig. 4d shows a gradual increase in the vibrational peak of gaseous NO (1909 cm^{-1}) over time, indicating the presence of NO_2^- intermediates[46]. As shown in Fig. 4e, f, these peaks disappear within 5 minutes upon the introduction of N_2, demonstrating the rapid desorption of NO_2^- and gaseous NO from the catalyst surface.

In summary, our study presents a TiN-based gas sensor synthesized via ammonolysis of titanium cluster MOF **MIL-125**, featuring an ultra-high specific surface area (221.9 m²/g) and abundant NVs. This TiN-600 sensor exhibits exceptional selectivity for NO_2, with a response of 6.05 μA at 50 ppm, outperforming other interfering gases with a signal that is 30 times greater than that for NO. It also demonstrates reliable repetitive detection with long-term stability, showing minimal sensitivity drift of 4.2% over 6 months. Our TiN electrochemical gas sensor priced at US$0.08 g^{-1} is significantly more cost-effective than Pt-based sensors at US$30.15 g^{-1} (average prices in 2024)[47]. Utilizing in-situ FTIR and EPR, we have clarified the underlying NO_2 sensing mechanism. This work not only advances the development of high-performance gas sensing materials but also provides a direction for optimizing electrochemical gas sensors for practical environmental monitoring and industrial applications.

Methods

Sample preparation

MIL-125 (Ti) (MIL: Materials of Institute Lavoisier) was synthesized using a modified method based on the literature[23]. H_2BDC ($C_8H_6O_4$, 1000 mg, 6 mmol) and TTIP ($C_{12}H_{28}O_4Ti$, 864 mg, 0.9 mL, 3 mmol) were added to a solution of anhydrous DMF (25 mL) and methanol (25 mL). The mixture was stirred thoroughly at room temperature, then transferred to a 100 mL Teflon-lined autoclave and heated at 150 °C for 16 h. The resulting suspension was filtered, washed alternately with DMF and methanol three times, and dried to yield a white solid sample. Approximately 100 mg of **MIL-125** (Ti) powder was placed in a ceramic boat inside a tube furnace. Using NH_3 as the flowing gas (flow rate of 100 cm³/min), the temperature was raised at a rate of 5 °C/min to the target temperature (500–900 °C) and maintained for 3 h for heat treatment. After completion of the ammonolysis reaction, the sample was kept in the NH_3 atmosphere until the tube furnace cooled to room temperature. Finally, the sample is taken out of the tube furnace.

Material characterization

Powder X-ray diffraction (XRD) measurements were performed using a Bruker D8 Advance powder X-ray diffractometer with Cu Kα radiation (λ = 1.5418 Å). The specific surface area and microporous analysis for the TiN series samples were determined using a 3FLEX analyzer (USA) based on the Brunauer-Emmett-Teller (BET) method. Scanning Electron Microscopy (SEM) images were captured using a JSM-7900F instrument (Japan). High Resolution Transmission Electron Microscopy (HRTEM) imaging and Electron Energy-Loss Spectroscopy
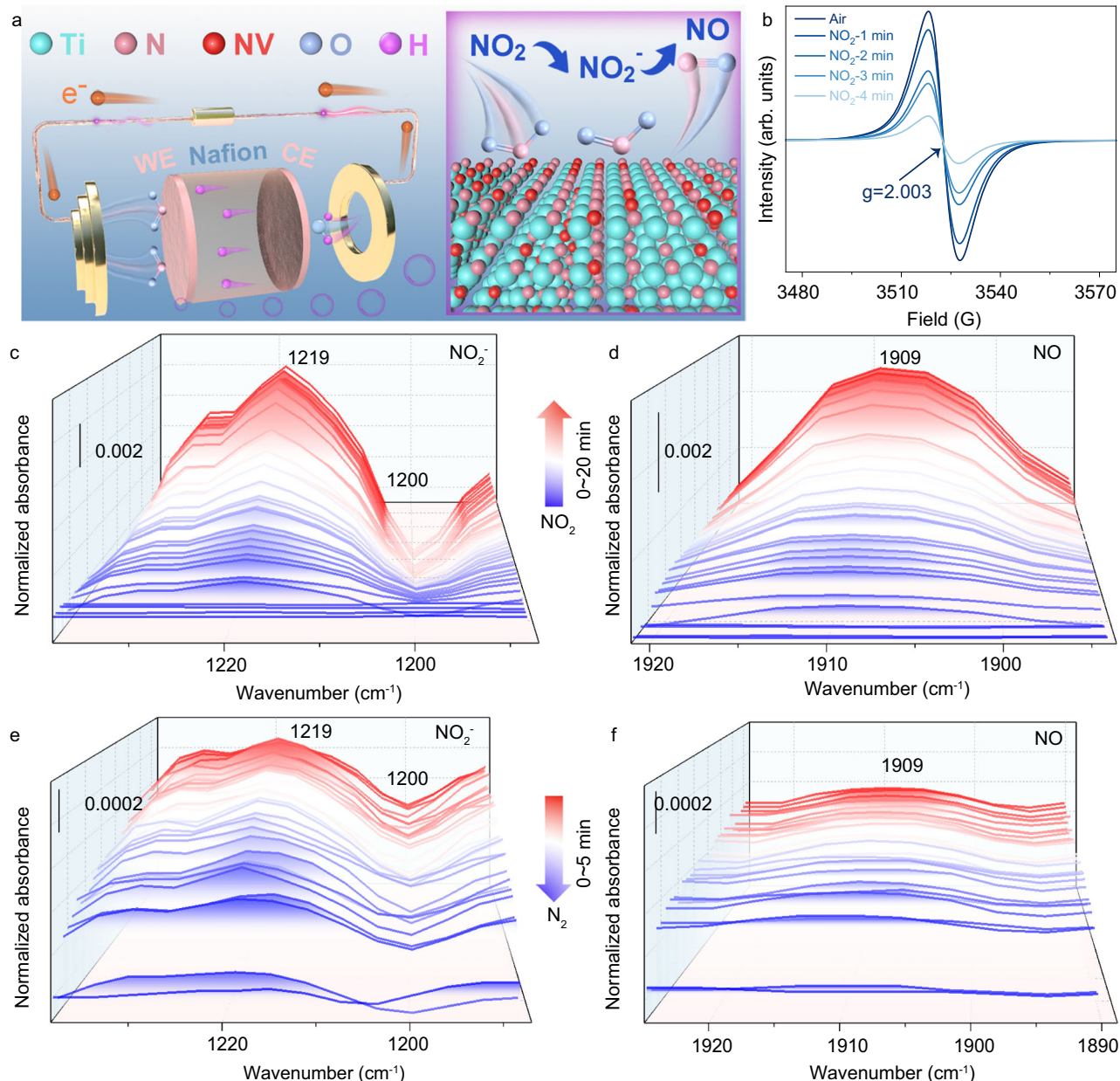
Fig. 4 | In situ characterization of the gas-sensing mechanism in TiN$_x$-based NO$_2$ sensors. a Schematic illustration of the structure and gas-sensing mechanism of the TiN-600 electrochemical gas sensor. NO$_2$ is first reduced to NO$_2^-$ at the working electrode (WE), then further reduced to NO. Electrons are transferred through the external circuit, generating the sensor's response signal. CE counter electrode. NV nitrogen vacancy. **b** In-situ Electron Paramagnetic Resonance (EPR) monitoring of TiN-600. **c, d** In-situ Fourier Transform Infrared Spectroscopy (FTIR) spectra recorded during the NO$_2$ sensing process on TiN-600. **e, f** In-situ FTIR spectra recorded after the introduction of N$_2$ on TiN-600. Source data are provided as a Source Data file.

(EELS) elemental mapping were conducted with Spectra 300 (TFS, USA) equipped with Super-X detector system. X-ray Photoelectron Spectroscopy (XPS) was performed using a Thermo Scientific K-Alpha+ spectrometer with Al Kα radiation under ultrahigh vacuum, and the binding energy was calibrated using the C 1s peak (284.8 eV). Transmission X-ray Absorption (XAS) measurements were obtained using the easy XAFS300 laboratory system from easy XAFS LLC, which includes Rowland circle geometries, spherically bent crystal analyzers (SBCA), and a silicon drift detector. The in-situ Fourier transform infrared (FTIR) was tested using an MCT detector (Bruker VERTEX 70). Electron Paramagnetic Resonance (EPR) spectroscopy was used to examine the NVs in the TiN series samples, utilizing a Bruker A200-9.5/12 instrument.

Preparation of gas sensor

The gas sensor is prepared according to the further improvement of the reported literature[20]. The actual image of the core component, the membrane electrode assembly (MEA), is shown in Fig. S28. It has a diameter of approximately 10 mm and a thickness of approximately 0.5 mm. The preparation method is as follows: 5 mg of TiN powder, 40 μL of Nafion solution (5 wt%, DuPont, USA), and 460 μL of isopropanol were ultrasonically treated to form a catalyst ink, which was then drop-cast onto the surface of carbon paper at 90 °C. Subsequently, the Nafion N-115 membrane (DuPont, USA) was sandwiched between two sheets of carbon paper and protected with two Polytetrafluoroethylene (PTFE) membranes, then hot-pressed at 90 °C and 1 MPa for 120 s. Finally, the PTFE membranes were peeled off to obtain the MEA.

Gas preparation method

In this work, we employed a method that combines a dynamic gas mixing system (Fig. S29) with a static gas preparation technique (Fig. S30). Initially, a flow meter accurately controlled the flow of ppm-level NO_2 and purified air into a mixing chamber of approximately 1 L, ensuring thorough mixing. The resulting gas then exited through the outlet at the opposite end, achieving the desired concentration. The method used for mixing other interfering gases mirrors that of NO_2. The concentration of the prepared standard gas is calculated using the following formula:

$$C_1 = C_0 \cdot \frac{Q_0}{Q + Q_0} \quad (4)$$

where C_1 is the gas concentration obtained using the dynamic gas mixing method (ppm), C_0 is the initial concentration of test gas (ppm), Q_0 is the flow rate of NO_2 (mL/min), and Q is the flow rate of air (mL/min). To prepare test gases at ppm -level (≥ 1 ppm), the dynamic gas mixing method facilitates direct dilution. However, achieving ppb-level concentrations of NO_2 is challenging with just a dynamic gas mixing system and flow meter, requiring the integration of a static gas preparation method. This process begins with a gas source at concentration C_1 derived from the dynamic method. First, a 20 L glass bottle is cleaned and dried at atmospheric pressure. It is then evacuated and purged several times with purified air before another evacuation. A specific volume of NO_2 at concentration C_1 is injected, and purified air is added to bring the bottle to atmospheric pressure. The bottle is shaken and allowed to rest to ensure uniform mixing. The concentration of the standard gas is calculated using the following formula:

$$C_2 = \frac{C_1 \cdot V_1}{V_2} \quad (5)$$

where C_2 is the final concentration of NO_2, V_1 is the volume of NO_2 injected, and V_2 is the volume of the gas bottle. The combination of the two gas mixing methods ensures the reliability of gas concentration ranging from 50 ppm to 50 ppb. In this study, the source gas is 200 ppm NO_2 (purity of 99.999%, diluted with high-purity N_2). The background gas used for testing is high-purity air.

Gas sensing measurements

The gas sensitivity performance of the sensor is evaluated by recording the current changes of the sensor in different concentrations and types of gases. The sensor response is defined as $\Delta I = I - I_0$, where I_0 and I represent the current of the sensor in atmospheric air/N_2 and the target gas, respectively.

Data availability

The data supporting the findings of this study are reported in the main text or the Supplementary Information. Source data are provided with this paper and in the figshare database with the link: https://doi.org/10.6084/m9.figshare.27175389. Source data are provided with this paper.

References

1. U. S. Environmental Protection Agency. *Setting and Reviewing Standards to Control NO₂ Pollution*; https://www.epa.gov/no2-pollution/setting-and-reviewing-standards-control-no2-pollution (accessed 23 Oct 2024).
2. World Health Organization. *Air Quality, Energy and Health*; https://www.who.int/teams/environment-climate-change-and-health/air-quality-and-health/health-impacts/types-of-pollutants (accessed 23 Oct 2024).
3. Cooper, M. J. et al. Global fine-scale changes in ambient NO₂ during COVID-19 lockdowns. *Nature* **601**, 380–387 (2022).
4. World Health Organization. *Billions of People Still Breathe Unhealthy Air: New WHO Data*; https://www.who.int/news/item/04-04-2022-billions-of-people-still-breathe-unhealthy-air-new-who-data (accessed 23 Oct 2024).
5. U.S. Environmental Protection Agency. *Nitrogen Dioxide (NO₂) Standards-Table of Historical NO₂ NAAQS*; https://www3.epa.gov/ttn/naaqs/standards/nox/s_nox_history.html#3 (accessed 23 Oct 2024).
6. Li, Q., Zeng, W. & Li, Y. Metal oxide gas sensors for detecting NO₂ in industrial exhaust gas: recent developments. *Sens. Actuators B Chem.* **359**, 131579 (2022).
7. Shin, S. et al. Carbon-embedded Pt alloy cluster catalysts for proton exchange membrane fuel cells. *Adv. Energy Mater.* **14**, 2400599 (2024).
8. Yu, K. et al. Degradation mechanisms of platinum nanoparticle catalysts in proton exchange membrane fuel cells: the role of particle size. *Chem. Mater.* **26**, 5540–5548 (2014).
9. Geng, X. et al. Atomically dispersed Pb ionic sites in PbCdSe quantum dot gels enhance room-temperature NO₂ sensing. *Nat. Commun.* **12**, 4895 (2021).
10. Ou, Y. et al. Crystal face-dependent behavior of single-atom Pt: construct of SA-FLP dual active sites for efficient NO₂ detection. *Adv. Sci.* **11**, 2402038 (2024).
11. Wang, H. et al. Transition metal nitrides for electrochemical energy applications. *Chem. Soc. Rev.* **50**, 1354–1390 (2021).
12. Huang, C., Zhao, J., Qu, F., Wang, J. & Yang, M. A fuel cell type gas sensor based on Pt/NbN for highly selective detection of hydrogen sulfide. *Sens. Actuators B Chem.* **346**, 130516 (2021).
13. Huang, C. et al. Low platinum catalyst supported on titanium molybdenum nitride for efficient CO sensing. *Sens. Actuators B Chem.* **364**, 131917 (2022).
14. Huang, C. et al. Mesoporous titanium niobium nitrides supported Pt nanoparticles for highly selective and sensitive formaldehyde sensing. *J. Mater. Chem. A* **9**, 19840–19846 (2021).
15. Mo, X. et al. Nitrogen-doped indium oxide electrochemical sensor for stable and selective NO₂ detection. *Adv. Mater.* **36**, e2409294 (2024).
16. Cheng, Z. et al. Recent advances in transition metal nitride-based materials for photocatalytic applications. *Adv. Funct. Mater.* **31**, 1–22 (2021).
17. Barragan, A. A. et al. Photochemistry of plasmonic titanium nitride nanocrystals. *J. Phys. Chem. C.* **123**, 21796–21804 (2019).
18. Galuskin, E. et al. FirstIn situterrestrial osbornite (TiN) in the Pyrometamorphic Hatrurim Complex, Israel. *Lithosphere* **2022**, 8127747 (2022).
19. Guan, H. et al. General molten-salt route to three-dimensional porous transition metal nitrides as sensitive and stable Raman substrates. *Nat. Commun.* **12**, 1376 (2021).
20. Huang, C. et al. Mesoporous Ti₀.₅Cr₀.₅N for trace H₂S detection with excellent long-term stability. *J. Hazard Mater.* **423**, 127193 (2022).
21. Yuan, Y. et al. Zirconium nitride catalysts surpass platinum for oxygen reduction. *Nat. Mater.* **19**, 282–286 (2019).
22. Horvath-Bordon, E. et al. High-pressure chemistry of nitride-based materials. *Chem. Soc. Rev.* **35**, 987–1014 (2006).
23. Dan-Hardi, M. et al. A new photoactive crystalline highly porous titanium(IV) dicarboxylate. *J. Am. Chem. Soc.* **131**, 10857–10859 (2009).
24. Jin, H. et al. Nitrogen vacancies on 2D layered W₂N₃: a stable and efficient active site for nitrogen reduction reaction. *Adv. Mater.* **31**, 1902709 (2019).
25. Wu, Y. et al. Regulating the interfacial electronic coupling of Fe₂N via orbital steering for hydrogen evolution catalysis. *Adv. Mater.* **32**, 1904346 (2020).
26. Ye, Z., Jiang, Y., Li, L., Wu, F. & Chen, R. Synergetic anion vacancies and dense heterointerfaces into bimetal chalcogenide nanosheet

arrays for boosting electrocatalysis sulfur conversion. *Adv. Mater.*
34, 2109552 (2022).

27. Liu, G. et al. Cation-assisted formation of porous TiO_{2-x} nanoboxes with high grain boundary density as efficient electrocatalysts for lithium-oxygen batteries. *ACS Catal.* **8**, 1720–1727 (2018).

28. Peng, C. et al. Double sulfur vacancies by lithium tuning enhance CO_2 electroreduction to n-propanol. *Nat. Commun.* **12**, 1580 (2021).

29. Li, X. et al. Selective visible-light-driven photocatalytic CO_2 reduction to CH_4 mediated by atomically thin $CuIn_5S_8$ layers. *Nat. Energy* **4**, 690–699 (2019).

30. Luo, Z. et al. Chemically activating MoS_2 via spontaneous atomic palladium interfacial doping towards efficient hydrogen evolution. *Nat. Commun.* **9**, 2120 (2018).

31. Rad, A. S., Nasimi, N., Jafari, M., Shabestari, D. S. & Gerami, E. Ab-initio study of interaction of some atmospheric gases (SO_2, NH_3, H_2O, CO, CH_4 and CO_2) with polypyrrole (3PPy) gas sensor: DFT calculations. *Sens. Actuators B Chem.* **220**, 641–651 (2015).

32. Du, H. et al. Enhancement of NO_2 gas sensing properties of polypyrrole by polarization doping with DBS: experimental and DFT Studies. *ACS Appl. Mater. Interfaces* **15**, 52961–52970 (2023).

33. Zhao, X. et al. High-performance H_2S sensors to detect SF_6 leakage. *ACS Sens.* **9**, 5512–5519 (2024).

34. Meng, D. et al. Pt/WN-based fuel cell type methanol sensor. *Sens. Actuators B Chem.* **307**, 127686 (2020).

35. Liu, S., Yu, B., Zhang, H., Fei, T. & Zhang, T. Enhancing NO_2 gas sensing performances at room temperature based on reduced graphene oxide-ZnO nanoparticles hybrids. *Sens. Actuators B Chem.* **202**, 272–278 (2014).

36. Zhang, M., Yuan, Z., Song, J. & Zheng, C. Improvement and mechanism for the fast response of a Pt/TiO_2 gas sensor. *Sens. Actuators B Chem.* **148**, 87–92 (2010).

37. Rong, Q., Lei, W., Huang, J. & Liu, M. Low temperature tolerant organohydrogel electrolytes for flexible solid-state supercapacitors. *Adv. Energy Mater.* **8**, 1801967 (2018).

38. Huang, L. et al. Expanding the range of trackable environmental pollutants for Nafion based fuel cell type gas sensor. *Sens. Actuators B Chem.* **399**, 134808 (2024).

39. Maia, L. B. & Moura, J. J. How biology handles nitrite. *Chem. Rev.* **114**, 5273–5357 (2014).

40. Kumar, K. V., Preuss, K., Titirici, M. M. & Rodriguez-Reinoso, F. Nanoporous materials for the onboard storage of natural gas. *Chem. Rev.* **117**, 1796–1825 (2017).

41. Getman, R. B., Bae, Y. S., Wilmer, C. E. & Snurr, R. Q. Review and analysis of molecular simulations of methane, hydrogen, and acetylene storage in metal-organic frameworks. *Chem. Rev.* **112**, 703–723 (2012).

42. Islamoglu, T. et al. Metal-organic frameworks against toxic chemicals. *Chem. Rev.* **120**, 8130–8160 (2020).

43. Zhang, J. et al. Embedded nano spin sensor for in situ probing of gas adsorption inside porous organic frameworks. *Nat. Commun.* **14**, 4922 (2023).

44. Nguyen, H. P., Palma Del Valle, S. & Marie, O. NO adsorption on K and Ba loaded on zirconia-titania NSR catalysts: a comparative study by in situ and operando IR spectroscopy. *Appl. Catal. B-Environ.* **231**, 391–399 (2018).

45. Venkov, T., Hadjiivanov, K. & Klissurski, D. IR spectroscopy study of NO adsorption and $NO + O_2$ co-adsorption on Al_2O_3. *Phys. Chem. Chem. Phys.* **4**, 2443–2448 (2002).

46. Zhang, R., Luo, N., Yang, W., Liu, N. & Chen, B. Low-temperature selective catalytic reduction of NO with NH_3 using perovskite-type oxides as the novel catalysts. *J. Mol. Catal. A Chem.* **371**, 86–93 (2013).

47. London Metal Exchange. https://www.lme.com/Metals/Precious/LBMA-Platinum#Annual+averages (accessed 8 Jun 2024).

Author contributions
X.Z. and M.Y. conceived the project. X.Z. carried out the sample synthesis, performance testing, and most of the sample characterization. Z.Z. performed the theoretical calculations. Z.X. and Y.Z. conducted the HAADF-STEM and EDS characterizations. J.L. performed the XAS and in-situ FTIR spectroscopy measurements. X.Y. analyzed the structure and composition of the samples. X.Z., J.P.A., and M.Y. wrote and revised the manuscript. All authors contributed to the scientific discussions and manuscript revisions.

Competing interests
The authors declare no competing interests.

Additional information
Supplementary information The online version contains supplementary material available at https://doi.org/10.1038/s41467-024-55534-x.

Correspondence and requests for materials should be addressed to Minghui Yang.

Peer review information *Nature Communications* thanks Seong-Yong Jeong, Matteo Valt and the other, anonymous, reviewer(s) for their contribution to the peer review of this work. A peer review file is available.

Reprints and permissions information is available at http://www.nature.com/reprints

Publisher's note Springer Nature remains neutral with regard to jurisdictional claims in published maps and institutional affiliations.